Research Article | Vol. 27, No. 16 | 5 Aug 2019 | OPTICS EXPRESS A1084

Optics EXPRESS

Characterization of underwater scattering layers based on variance components of LiDAR backscattering

Martin A. Montes,[1,2,3,*] Anni K. Vuorenkoski,[1] Fraser R. Dalgleish,[4] and Bing Ouyang[1]

[1]*Ocean Visibility and Optics Lab, Harbor Branch Oceanographic Institute, Florida Atlantic University, Fort Pierce, FL 5600, USA*
[2]*NASA Goddard Space Flight Center, Terrestrial Information Systems Laboratory, Greenbelt, MD 20771, USA*
[3]*Science Systems and Applications Inc. (SSAI), Lanham, MD 20706, USA*
[4]*Photonics and Quantum Sciences Technology Center, Space and Intelligent Systems, Harris Corporation, Palm Bay, FL 32905, USA*
[*]*martin.a.montes@nasa.gov*

Abstract: Range-resolved detection of submerged scattering layers was investigated in the Gulf of Mexico based on vertical profiles made with a LiDAR (Light detection and range) system having a green laser (wavelength λ = 532 nm). The backscattering power (S_d) variability was decomposed in principal components (PCs) and related to non-polarized S_d, the S_d ratio between cross- and co-polarized waveforms, the chlorophyll-a fluorescence (Fchl), and the ratio between volume scattering angles of 150° and 100°. The variance of PCs was dominated by non-polarized S_d followed by Fchl. Correlation between PC1 scores and Fchl anomalies suggested that S_d was mainly originated from pigmented particulates.

1. Introduction

The identification of spatial discontinuities in the ocean has important implications in marine optics because accuracy of remote sensing products derived from passive optical measurements (e.g., chlorophyll-a concentration) are very sensitive to vertical and horizontal changes on patchiness [1]. Also, thin optical submarine layers (e.g., < 1 m thick) have been proposed as important ecological niches where biogeochemical processes are intensified [2]. Lastly, the detection and discrimination of subsurface optical anomalies is relevant for military countermeasures (e.g., localization of mines and submarines) [3].

An important virtue of measuring systems in the last two applications is the capability of finding several targets and characterizing their composition in a quasi-simultaneous way and at some distance from the sensor to minimize instrument-induced perturbations. In that regard, multi-beam acoustic methods provide a relatively coarse spatial resolution with respect to optical techniques based on range-resolved LiDAR (Light detection and range) [4]. Likewise, unlike sound measurements, time-resolved LiDAR backscattering and fluorescence waveforms can be combined for performing the recognizance of the object under investigation [5]. Lastly, another important difference with acoustic approaches is that LiDAR probes are less invasive for detecting submerged features since they can be used from aerial or space platforms [6]. Unlike range-resolved LiDAR systems, the use of in situ vertical profilers (e.g., Argos floats, optical package in rosette) for mapping submarine optical layers is intrusive and prone to several sampling artifacts (e.g., non-steady water pumping, uneven depth measurements) [7]. Likewise, LiDAR determinations may include additional system parameters (e.g., vertical and horizontal scanning, polarization and variable Field-of-View or FOV) that can be applied to improve the discrimination of layers.

#352358 https://doi.org/10.1364/OE.27.0A1084
Journal © 2019 Received 18 Dec 2018; revised 24 Jan 2019; accepted 12 Feb 2019; published 10 Jul 2019

Optics EXPRESS

The detection of layers based on range-resolved LiDAR measurements are commonly performed based on signal slope changes and thresholds [8,9]. Most of these techniques have been designed for detecting and characterizing atmospheric layers based on spaceborne LiDAR [9,10]. The slope method is not sensitive to LiDAR system calibration changes even though is prone to large errors due to the presence of signal spikes and/or gradients within the internal structure of the optical layer. The implementation of thresholds and anomalies generally involves the background noise subtraction and are particularly reliable for those cases where the signal/noise ratio is high. The signal background subtraction can be achieved based on different methods (e.g., a linear regression model of log-transform backscattering [11].

The objective of this study is to test a deconvolution technique based on principal component analysis (PCA) for detecting and characterizing submarine scattering layers based on range-resolved LiDAR backscattering waveforms and independent ancillary information derived from fluorescence and angular scattering measurements. The layer detection/discrimination algorithm was developed with vertical profiles obtained by an underwater LiDAR system (FSUIL or Fine Structure Underwater Imagining LiDAR) in coastal waters of the Gulf of Mexico during March of 2016. This study is divided in three main sections. In the first section, different families of wavelets are evaluated for reducing the noise of LiDAR waveforms. In the second section, PCA orthogonal modes were related to LiDAR backscattering for three polarization states (non-polarized, linear cross-polarized and linear co-polarized components) and concurrent measurements related to chlorophyll-a fluorescence (Fchl) and angular changes on volume scattering function (β^r). Lastly, principal components of variance were applied to compute fine spatial resolution of range-resolved anomalies, and the performance of the PCA technique for detecting and discriminating scattering layers was investigated at different stand-off ranges and water turbidities. Also, the influence of vertical changes on water optical composition and multiple scattering effects on layer localization and identification was examined and discussed.

2. Methodology

2.1. LiDAR configuration

FSUIL is a near-monostatic pulsed laser scanning system developed at Harbor Branch Oceanographic Institute [12] (Fig. 1). The LiDAR can obtain information at 3 angles with respect to the zenith (0, 90 and 180°) from a specific location in the water column and have a 0.5° azimuthal resolution angles (Fig. 1(a)). FSUIL has a green laser (λ = 532 nm) with a divergence beam angle of 1 mrad, a 2-D scanner, and a receiver assembly with four 50 mm diameter telescopes. The receivers encompass two non-polarized (ch_1 and ch_4) and two polarized (ch_2 and ch_3) channels. Two FOVs controlled by a fixed iris were used (75.7 mrad for ch_1, ch_2 and ch_3, and 15 mrad for ch_4). Each telescope has a bandpass filter centered at 532 nm (3 nm at full width-half-maximum, FWHM, diameter = 50 mm), an F/2 plano-convex lens, a field stop iris, and a high speed photomultiplier tube (PMT) detector (Hamamatsu R9880U-210).

Optics EXPRESS

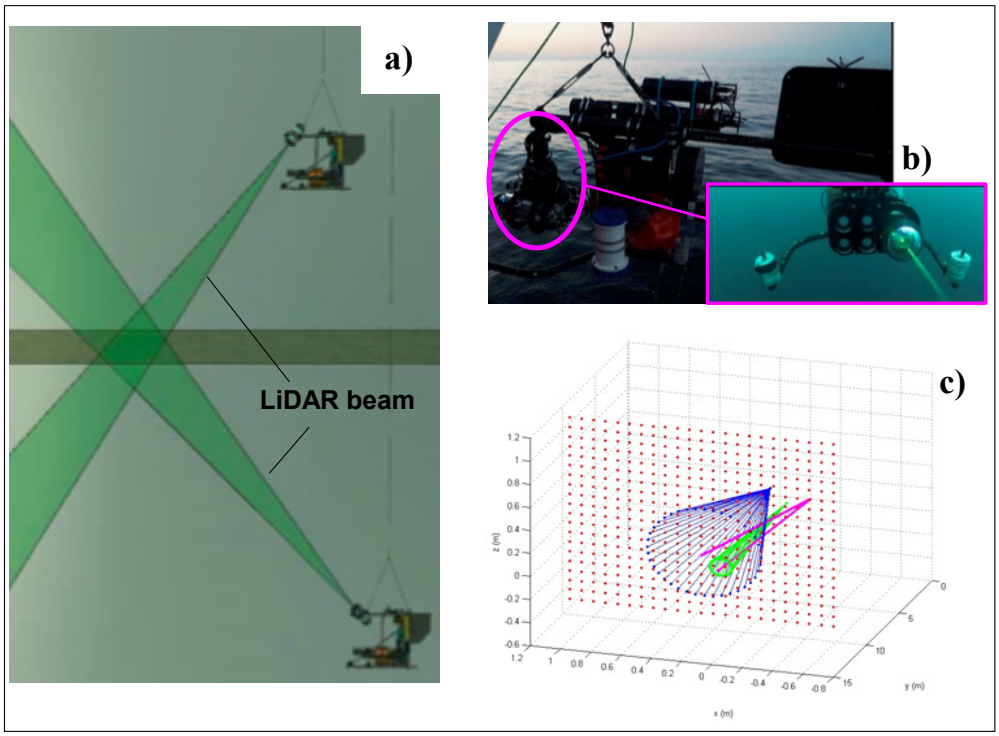

Fig. 1. FSUIL system. A) deployment and two shooting configurations (upper and lower cartoon), b) Optical package and LiDAR in operation (lower right picture), and c) 3-D scanning geometry of FSUIL. A matrix of 23 (width) x 20 (height) pulses is laying over the target plane (red dots) and is partially intersected by the common scattering volume of each receiver. ch_1 (blue lines) and ch_4 (green lines). Pulse with the maximum intensity (magenta lines).

The source-detector distance of ch_2 and ch_3 (0.266 m) is larger with respect to that of ch_1 1 and ch_4 (0.157 m). The energy of each pulse has a Gaussian spatial profile, a pulse duration at FWHM of 0.5 ns, and an energy of 20 μJ. The scanning area contains 460 pulses and covers an area of 1.7399 m (width) x 1.5748 m (height) at 10.45 m from the detector. The scanning pulse grids are created by swiping the laser beam from left to right for odd rows and vice-versa at consecutive even rows. The angular inter-pulse separation is 0.34° and the pulse repetition frequency is 500Hz. Time-resolved linear intensity measurements with 12-bit resolution (S) were obtained for each pulse. Intensity values were converted to voltage with a digitizer from SPDevices (ADQ-12) after manually applying specific gains for each receiver. The gains were constant during the whole survey and the waveforms were archived at 12-bit resolution. For each channel, each waveform was originally digitized in 256 time bins (hereafter absolute time bins).

2.2. Signal processing

The approach proposed in this study for remote detection of submarine layers is based on variance decomposition of waveforms, thus resulting variability modes are expected to be strongly affected by sensor saturation events and noise derived from different sources (systematic and non-systematic) that must be removed before applying the inversion method described in section in 2.6.

Sensor saturation events were sometimes observed and were thought to be caused by local backscattering spikes, which in severe cases leads to an observed ringing effect. This phenomenon was associated with the presence of high-reflective targets (i.e., ‘hard’ targets)

Optics EXPRESS

intercepting the laser beam. This signal saturation was empirically detected based on a full width at half maximum (FWHW) value of 2.5 ns. The noise of time-resolved LiDAR backscattering measurements was reduced by filtering the original waveforms without high-reflective targets with continuous wavelet transforms. Negative values in original waveforms were removed by adding an offset of 20 units to the raw data which is ac-coupled.

The wavelet is a wave-like oscillation that begins and ends at zero and that can be used to extract information of data sets having a finite domain and sharp discontinuities. Similar to Fourier, a wavelet function is a superposition of functions; however, the scale of the phenomenon is a critical concept for a wavelet representation. A general expression for a discrete wavelet function is:

$$\mathrm{W(x)} = \sum_{k}^{N-2} (-1)^k c_{k+1} \phi(2x+k) \tag{1}$$

$$\phi(\mathrm{s,l}) = 2^{-s/2} \phi(2^{-s} x - 1) \tag{2}$$

where W(x) is the scaling function for the mother wavelet ϕ, and c_k are the wavelet coefficients. The parameters s and l are integers that scale and dilate the original mother function. In this study, four different families of continuous wavelets were evaluated: Coiflets, Daubechies, Symlets and biorthogonal (hereafter coif, db, sym and bior, respectively) [13]. Wavelet families coif and sym (db and bior) are near (far from) symmetry. Another important difference between the selected wavelets is the number of vanishing moments (e.g., 2Nw for coif, Nw for db, where Nw is the order of the wavelet).

The calculations were made using scripts implemented in Matlab R2015b and the wavelet toolbox. A common initial setting in all wavelets was the use of a soft threshold based on Donoho and Johnstone's universal rule and a rescaling using level-dependent estimates of noise. For each detector, the mother wavelet having the highest correlation with the original raw signal was selected for denoising the LiDAR waveforms before the variance deconvolution [14] (see section 2.6). The Spearman rank correlation coefficient (ρs) [15] was chosen for comparisons of filtered and unfiltered backscattering signals. For each channel, the correlations were made based on seven waveforms measured within a range of water depths (34.07-61.5 m) and turbidities (beam attenuation coefficient at λ = 532 nm, c = 0.31-1.25 m^{-1}). For the sake of simplification, the wavelength notation of each optical parameter is not included in the remaining sections of the manuscript. The number of decomposition levels for each wavelet family was optimized based on the maximum value of ρs.

The noise suppression by wavelets was examined by calculating the Discrete Fourier Transform (DFT) of the initial (i.e., absolute time bins 1 to 30) and terminal (absolute time bins 156 to 256 and 200 to 256 for 'turbid' and 'clear' water cases, respectively) portions (hereafter off-water and in-water noise, respectively) of raw and denoised waveforms derived from cross and co-polarized channels. In all cases, the DFT was calculated after detrending the data sets. Five waveforms were selected for each water turbidity case (i.e., 'clear water', c = 0.24 to 0.27 m^{-1}, water depth = 30.85 to 30.88 m, 'turbid water', c = 0.98 to 1.38 m^{-1}, water depth = 55.6 to 58.3 m). A stationary behavior was assumed (i.e., a critical approximation of DFT) for each time series, thus the DFT of off-water noise was computed by merging 5 data sets for each water turbidity case study and FSUIL receiver. The power spectra of in-water noise in-water was computed based on individual waveforms.

2.3. LiDAR backscattering model

The propagation of each LiDAR pulse through an aqueous optical medium is associated to two physical phenomena: 1) beam spreading and 2) exponential attenuation of energy. These LiDAR propagation processes are expected to influence the deconvolution technique proposed here, thus their effects are indirectly examined based on water turbidity changes.

Optics EXPRESS

The LiDAR equation can be represented with the following equation [16,17]:

$$S_d(z) = S_t \eta \rho F_p A_d \cos^2(\theta) E N^{-1} \tag{3}$$

$$E = e^{-2\varsigma(b,\omega_o,\theta)Kz} \tag{4}$$

$$N = 2\pi z^2 \tag{5}$$

where S_d is the received optical peak power in m^{-1} sr^{-1}, S_t is the transmitted optical peak power in m^{-1} sr^{-1}, η is the optical efficiency of the receiving optics (dimensionless), F_p is the FOV loss factor (dimensionless), A_d is the aperture area of the receiver optics in m^2, θ is the off-nadir transmitted angle (°), ς is a pulse stretching factor (dimensionless) that depends on the total scattering coefficient (*b*), the single scattering albedo (ω_o) and θ. K is the diffuse attenuation coefficient (m^{-1}), and z is the range in m. Notice that the product $\varsigma(b,\omega_o,\theta)$ K is equivalent to K_{sys} or the LiDAR attenuation coefficient. Thus, K_{sys} includes multiple scattering effects due to changes on ς [18].

The F_p is also known as the overlap function and describes how scattered transmitted energy is arriving to the detector as a function of range [19]. F_p values vary between 0 and 1 when scattered photons are completely out or fully inside the FOV, respectively. Based on tank experiments [20], F_p was 1 (i.e., backscattered energy originated inside the scattering common volume) in ch_1, ch_2 and ch_3 when the range was 3.83, 2.72 and 3.94 m, respectively. F_p estimates in ch_4 were not possible due to the variability of the backscattered energy at very low turbidities (i.e., $c = 0.045$ m^{-1}).

2.4. In situ measurements

The sampling of optical variables derived from LiDAR and additional instruments (i.e., absorption-attenuation and scattering –meters) was performed in coastal waters of the Gulf of Mexico during March of 2016. A total of 14 study sites encompassing day- and nighttime profiles were investigated even though only one cast during March 22 was selected for testing the layer detection algorithm due to three reasons. Firstly, the LiDAR measurements encompassed a wide range of water depth and allowed the study of optical layers near the surface (i.e., < 5 m depth).

Thus, this information can be also used to validate range-resolved waveforms derived from spaceborne sensors (e.g., CALIOP or Cloud-Aerosol Lidar with Orthogonal Polarisation). Secondly, LiDAR measurements during that date were obtained upward-looking (i.e., zenith shooting angle), thus it allowed a further comparison with concurrent shipboard LiDAR measurements (Shipboard Optical LiDAR Profiler, SLOP, Naval Research Lab, Alan Weidemann).Lastly, the chosen FSUIL data set had a minimum time difference (i.e., 21 minutes) with vertical profiles of inherent optical properties obtained by another research team. During March 22, the LiDAR instrument was deployed in an ascending continuous mode during daylight conditions (local time between16:55 and 17:16 pm). The contribution of ambient light to LiDAR backscattered power was minimized by using 50 mm interference filters (FWHM = 5 nm, center wavelength 532 ± 1 nm, out of band rejection PD6, Materion Inc.). Also, strong LiDAR returns near the sea-surface were eliminated due to signal contamination caused by retro-reflection of forward-scattered photons. Given the relatively slow ascending rate of the LiDAR instrument with respect to the shooting/detection rate, there was a depth overlap between consecutive range-resolved LiDAR waveforms.

LiDAR waveforms were always obtained with the same angular geometry (i.e., fixed laser pointing angles for each detector). The laser shot number corresponding to the maximum intensity was 311, 312, and 266 for detector 1, 2, and 3 respectively. The pulse position is determined based on a matrix of 20 (vertical) x 23 (horizontal) shots starting in the upper-left corner and finishing in the lower-right corner. LiDAR measurements were accompanied by concurrent (i.e.., backscattering coefficient at λ = 532 nm, b_b, Fchl, z, β at scattering angles ψs

Optics EXPRESS

of 100, 125 and 150° and λ = 532 nm) and non-concurrent (i.e.., absorption coefficient, *a*, and *c* at λ = 532 nm b_b at λ = 529 nm) depth profiles. This complementary information was used to develop the range-resolved layer detection algorithm and help to elucidate the composition of each scattering layer.

Raw total backscattering (i.e., water + particulates) determinations at 117° and λ = 532 nm were made using the optical package BBFL2 (sensitivity = 0.003 m^{-1} sr^{-1}, sampling rate = 8 Hz, WetLabs, Inc). Also, this sensor package allowed Fchl measurements (excitation λ = 465 nm, emission λ = 695 nm, sensitivity = 0.025 mg m^{-3}, range = 0-50 mg m^{-3}). Values of z were derived from a CTD sensor attached to the optical package (accuracy = ± 0.1%, Sea-Bird, Inc).

The angular variation of the volume scattering function was estimated from β(ψs1)/ β(ψs2) ratios, where ψs1 and ψs2 are computed at 150 and 100°, respectively. The measurements were made using a backscattering-meter ECO-VSF3 (WetLabs, Inc.) and with a sensitivity of 1.24 10^{-5} m^{-1} sr^{-1}. The calibration of β values was performed by the manufacturer by using 2 μm microspherical polystyrene beads (Duke scientific) [21]. The magnitude of the particulate backscattering coefficient (b_{bp}) was computed in two steps. Firstly, the pure seawater backscattering contribution at 117° (βw) was subtracted from total β in order to obtain βp. Lastly, b_{bp} was derived by multiplying βp by 2π χp, where χp is a wavelength-independent proportionality factor that was assumed to be 0.9 [22,23].

Calculations of b_b also involved two steps. Firstly, the pure seawater backscattering contribution to b_b (b_{bw}) was estimated from tabulated tables by multiplying the theoretical scattering coefficient of pure seawater (b_w) by 0.5 [24]. Lastly, b_b values were computed by summing b_{bw} and b_{bp} values as estimated above. Protocols for determining *a* and *c* values have been previously described [25]. The *b* was computed by subtracting *a* from *c* measurements. Also, the particulate scattering coefficient (b_p) was derived by subtracting the seawater contribution from *b* values. The particulate backscattering efficiency (b_{bp}^{eff}) was calculated by dividing b_{bp} by b_p. Likewise, ω_o at λ = 532 nm was determined by calculating the ratio *b*/*c*.

2.5. Multiple scattering effects

As the LiDAR pulse propagates away from the detector the number of scattering events and probability of extinction of photons increase. This phenomenon is enhanced at higher concentrations of particulates and associated water turbidities. To study the influence of multiple scattering on range-resolved detection and discrimination of optical layers, two parameters were calculated: the absolute (diff(c - K_{sys}) = c - K_{sys}) and relative (f(c - K_{sys}) = (c - K_{sys})/c) difference between *c* and K_{sys}, respectively. In general, diff(c - K_{sys}) and f(c - K_{sys}) increase at higher water turbidities as *c* changes are larger than K_{sys} changes As turbidity increases (decreases), the contribution of multiple scattering to total scattering (i.e., single + multiple) increases, and K_{sys} approaches the magnitude of K (*c*) [16,19].

The calculation of K_{sys} was based on denoised waveforms not including saturation events. For each channel, each K_{sys} value was derived every 5 ns as the slope of the linear regression function between the log-transformed backscattering signal and the range in m. For each waveform, the initial and ending of point of each group of K_{sys} estimates was 2.22 and 4.44 m from the laser source, respectively. The arithmetic average of K_{sys} values ($\langle K_{sys} \rangle$) for each shot was associated to the water depth of the FSUIL instrument (i.e., first range-resolved time bin) by substracting an offset of 1.34 m. Notice that the water depth is derived from the depth sensor integrated in the optical package measuring the ancillary variables (i.e., Fchl and β^r).

Values of $\langle K_{sys} \rangle$ were matched with *c* measurements by interpolating original values at 1 m vertical resolution.

Optics EXPRESS

2.6. Statistical analysis

Variance modes of denoised LiDAR waveforms derived from three FSUIL receivers were computed based on PCA [26]. Principal components (hereafter PCs) represent directions of maximum variability for a particular data set and are constructed as linear combinations that are independent one from each other (orthogonal). The main intention of PCA is the dimensionality reduction of the data. However, in our case, PCA was also applied to identify which modes of LiDAR-related backscattering variability can be used to detect and discriminate vertical discontinuities associated to uneven distribution and composition of particulates throughout the water column. For each waveform, only a subset of backscattering values corresponding to arriving times between 2.5 and 42.5 ns (i.e., 0.28-4. m away from the trigger, absolute time bins 40 to 121) were analyzed in order to avoid the small signal/noise ratios of the leading and trailing portions of each waveform. Also, an individual PCA calculation was performed for each time bin, thus a finer temporal resolution was achieved (i.e., 0.5 ns or 5.55 cm).

The selection of PCA variables was defined based on the following criteria. Firstly, the co-dependency among LiDAR waveforms measured by different receivers was minimized by reducing the number of channels since preliminary results suggested a major redundancy (> 90% of the total variance was explained by the first component) when four detectors were used. Secondly, ch_4 measurements were not included since time-resolved variability of backscattering was very irregular and did not show the typical maximum backscattering power within the common scattering volume. Thirdly, only concurrent ancillary optical information collected during the upward FSUIL profile was used to avoid temporal aliasing with respect to LiDAR measurements. Lastly, Fchl and β^r variables were chosen because their variability is linked to the origin of particulates in terms of size distribution and chemical composition (e.g., organic vs inorganic).

The calculation of PCA encompassed 5 steps: 1) merging of S_d values derived from j waveforms and for the relative time bin i (i.e., relative time bin 1 is equivalent to absolute time bin 40), 2) calculation of parameters derived from S_d (i.e., depolarization ratio index or DRI = S_d^{ch2}/S_d^{ch3}) and β^r, 3) z-transform of PCA input variables (i.e., $z = (v - \bar{v})/\sigma$, where $\bar{v}$ and σ are the arithmetic average and standard deviation of v, respectively, 4) matching of range-resolved LiDAR backscattering measurements with ancillary variables (i.e., β^r and Fchl) at 5.55 cm vertical resolution, and 5) variance decomposition in orthogonal components. Notice that there was only one waveform corresponding to the maximum intensity for each FSUIL depth position (i.e., no multiple shots from a specific vertical location).

The statistical analysis was divided in three sections. Firstly, the variability associated to DRI, Fchl and β^r was related to the PCA scores (i.e., coordinate of each point with respect to the principal component axes) corresponding to a specific time bin. The PCA correlation coefficients (Coeff), also known as loadings, were computed between PCs and parameters S_d^{ch1}, DRI, Fchl and β^r. Secondly, the contribution of each principal component (i.e., eigenvalues) to the total variance and as a function of range was computed in order to examine potential variations in the leading and trailing sections of waveform subsets (i.e.., relative time bins 1-20 and 70-81, respectively) due to multiple scattering effects. Lastly, the sign and magnitude of PC scores were studied for different scattering layers located at depths characterized by contrasting optical characteristics in terms of c and b_{bp}^{eff}.

3. Results

3.1. Noise reduction

In general, the magnitude of the Spearman correlation coefficient suggested that biorthogonal spline level 2 (bior3.5, low and high frequency band pass of 12 and 4, respectively) and

Optics EXPRESS

Daubechies level 8 (db8) wavelets were the most and least performing numerical filters to remove high frequencies linked to noise (green and blue curves, respectively, Fig. 7, Appendix). For ch_1 and ch_2, coiflets and symlets with 3 and 8 decomposition levels (i.e., coif3 and sym8, respectively) had only a substantial noise reduction at very high *c* values measured at depths greater than 50 m (Fig. 7(a)-7(b)). The reconstruction of 'free-noise' waveforms based on wavelets was usually higher for cross-polarized backscattering measurements ($\rho s > 0.95$ at all water depths, Fig. 7(c)).

Examples of raw and denoised time-resolved and polarized backscattering signals arriving to ch_2 and ch_3 receivers are illustrated in Fig. 2 for two contrasting water turbidities. 'Clear water' and 'turbid water' case studies corresponded to LiDAR shots made upward and from a water depth of 30.88 and 58.33 m, respectively. Notice that depth of *c* measurements is matching the water depth associated to the first relative time bin of range-resolved backscattering used for the PCA deconvolution.The signal trigger was present at 17 ns (i.e., absolute time bin = 34)in all waveforms and is more remarkable for relatively low *c* measurements as expected. Also, the effect of a high-reflective target (e.g., signal ringing) on LiDAR backscattering was clearly identified in raw and denoised waveforms arriving to ch_2 and when measurements were performed in relatively clear waters (Fig. 2(a)).

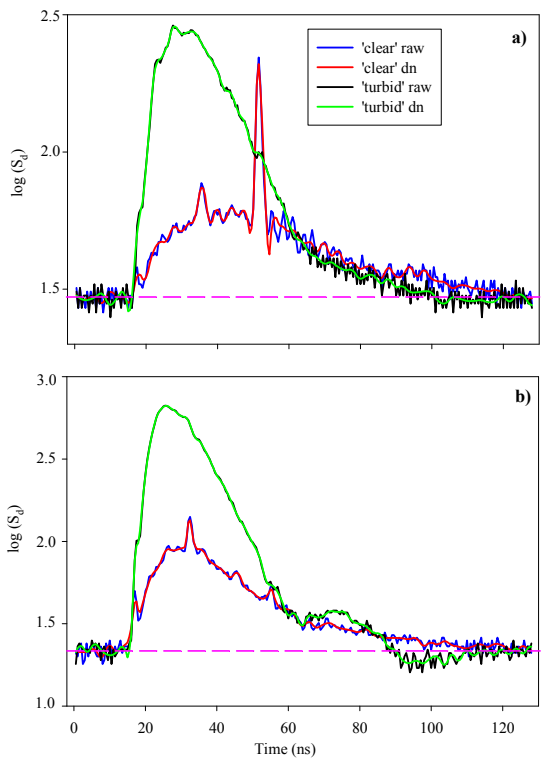

Fig. 2. Examples of raw and denoised LiDAR waveforms. a) ch_2, b) ch_3. Denoised waveforms (dn), mean noise (dash magenta line). LiDAR power at the receiver (S_d) is in log-scale. Trigger (T) and highly reflective targets (R).

As expected, the backscattering power of co- and cross-polarized channels increased at higher *c* values (Fig. 2(a)-(b)). Likewise, the decay of the backscattering power with range was larger at higher water turbidities. Due to this signal attenuation differences, spurious backscattering values (i.e., signal-to-noise ratio ≤ 1) for the 'turbid water' case were measured for samples collected later than 90 ns and 100 ns for ch_2 and ch_3, respectively. Noise also

Optics EXPRESS

dominated the initial portion of the waveform (i.e., first 15 ns). Indeed, the variability of LiDAR backscattering measured by ch_1 and ch_2 receivers was comparable between different water turbidities (Fig. 8). The power spectra (W) (i.e., square of Fourier transform) of the initial portion of waveforms (i.e., absolute time bins 1 to 30) arriving to both detectors were not influenced by water turbidity and was commonly characterized by a white noise distribution of energy (Fig. 9(a)-(b)). In general, the denoising of off-water noise in ch_2 and ch_3 decreased the energy of frequencies higher than 0.6 and 0.8 Ghz, respectively. For co- and cross-polarized receivers, the in-water noise of waveforms (i.e., backscattering power associated to the last 50 time bins) measured in 'clear waters' was in average higher with respect to that associated to waveforms obtained in 'turbid waters' (Fig. 10). Likewise, the power spectra of denoised waveforms for in-water noise showed a greater reduction of energy at frequencies above 0.3 Ghz (W decreased up to 5 decibels in ch_3) which is indicative of a low pass filtering effect from the PMT, which has the 3dB drop-off point at 0.25 GHz. (Fig. 10(c)-(d)).

3.2. Interpretation of PC components

PC1, PC2, PC3 and PC4 explained 63, 26, 10 and 1% of the total variance, respectively. An example of PC scores for the first relative time bin of each waveform subset is illustrated in Fig. 3.

Optics EXPRESS

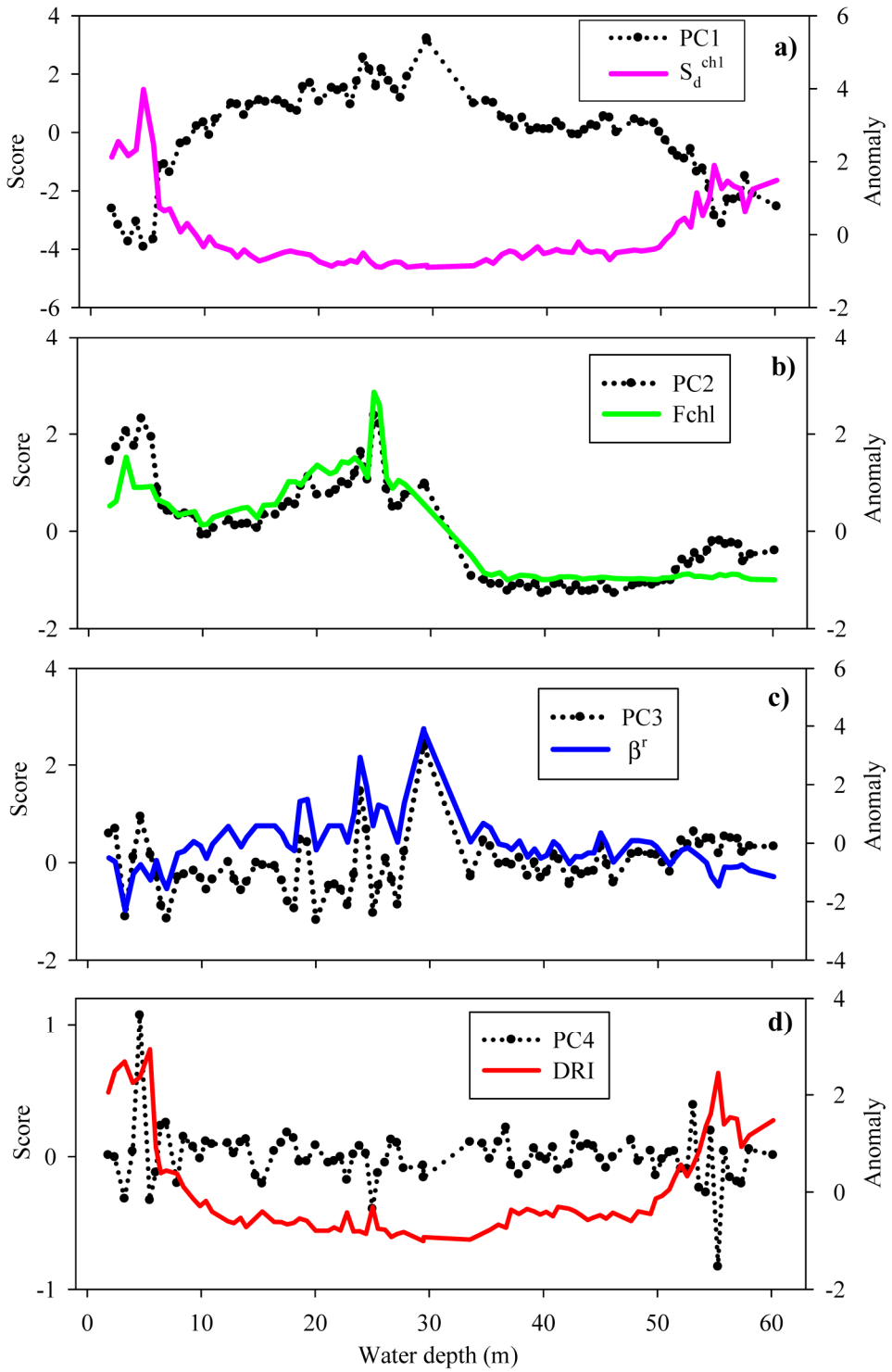

Fig. 3. Principal component scores and anomalies of optical parameters as a function of water depth. a) PC1 and S_d^{chl}, b) PC2 and Fchl, c) PC3 and β^r and d) PC4 and DRI; scores (left y-axis), anomalies (right y-axis).

Optics EXPRESS

Principal component scores showed that PC1 variability was strongly associated to anomalies of non-polarized backscattering (Coeff = –0.59) as denoted by the covariations observed at 4.6 and 54.8 m depth (Fig. 3(a)). PC2 was mainly explained by changes on chlorophyll-a fluorescence (Coeff = 0.89) (Fig. 3(b)). Direct correspondence between PC2 and Fchl was particularly strong at 3.3 and 25 m depth. Vertical variations of PC2 and anomalies of Fchl values were uncoupled at depths greater than 51.5 m. Variability of PC3 was mainly attributed to depth changes on β^r (Coeff = 0.82) (Fig. 3(c)). Large positive covariations between PC3 and anomalies of β^r were detected at 19.2, 24.2 and 29.5 m depth. Lastly, PC4 was principally related to anomalies of non-polarized backscattering and DRI (Coeff = –0.72 and 0.69, respectively) (Fig. 3(a)-(d)). The inverse covariation between PC4 and changes on DRI was well defined at 3.2, 4.6, 5.5, 25 and 55.3 m depth.

In general, the contribution of PC1 to total variance of vertical profiles tended to increase further away from the LiDAR detector but in the last 7 ns of each wavelet subset where a steady drop occurred (Fig. 4(a)). Notice that each bin includes information from different depths and water turbidities. Also, time-resolved plots depicted in Fig. 4 correspond to a relative time (tr) with respect to the first absolute time bin (i.e. 40 or t_0).

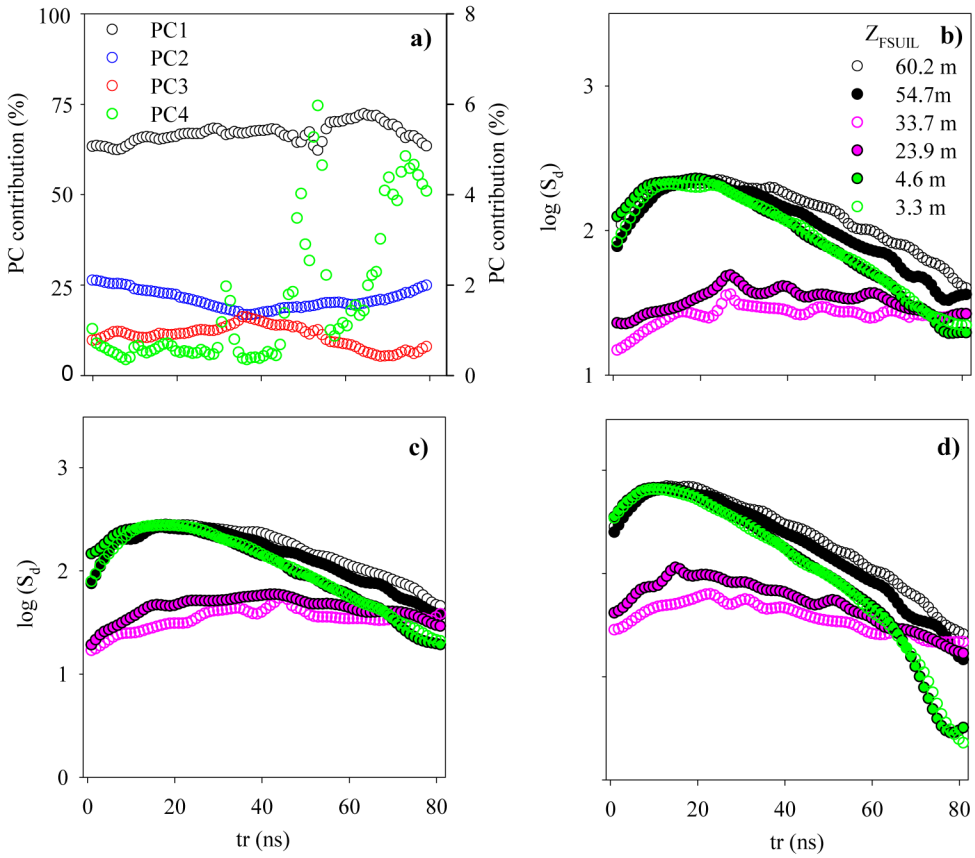

Fig. 4. Range-resolved variation of PC variance contribution as a function of relative time (tr). a) partial contribution of each PC (PC1-PC3, left axis, PC4, right axis), b) log-transformed denoised LiDAR waveforms for ch _1; data with (solid symbol) and without (empty symbol) scattering layers, c) and d) same as b) but for ch_2 and ch_3, respectively. Z_{FSUIL} is the instrument depth.

The variation of PC2 contribution showed a V pattern with values decreasing from tr 0 to 18.3 ns, and increasing from tr 18.3 to 40 ns. PC3 contribution with respect to different

Optics EXPRESS

positions along the waveforms mirrored the variations associated to PC2. Lastly, contribution of PC4 tended to increase with distance even though this monotonic variation was disrupted at time bins 15.4 and 26.3 ns (Fig. 4(a)). The slope break in PC1 contribution toward the last portion of the waveform was related to range-resolved changes of LiDAR backscattering (Fig. 4(b)(c)-(d)). This drastic variation occurred in non-polarized and polarized waveforms measured in turbid regions associated to surface or deep waters (i.e., green and black symbols, respectively). There was not a clear connection between waveform shapes and range-resolved variability of PC2, PC3 and PC4 contributions.

Case studies of principal components scores are shown in Fig. 5 for waveforms obtained at different distances of PC1-derived discontinuities situated near the surface (3.2 and 5.3 m), mid-depth (25.2 and 27.6 m) and deep (53.9 and 56.6 m) vertical locations.

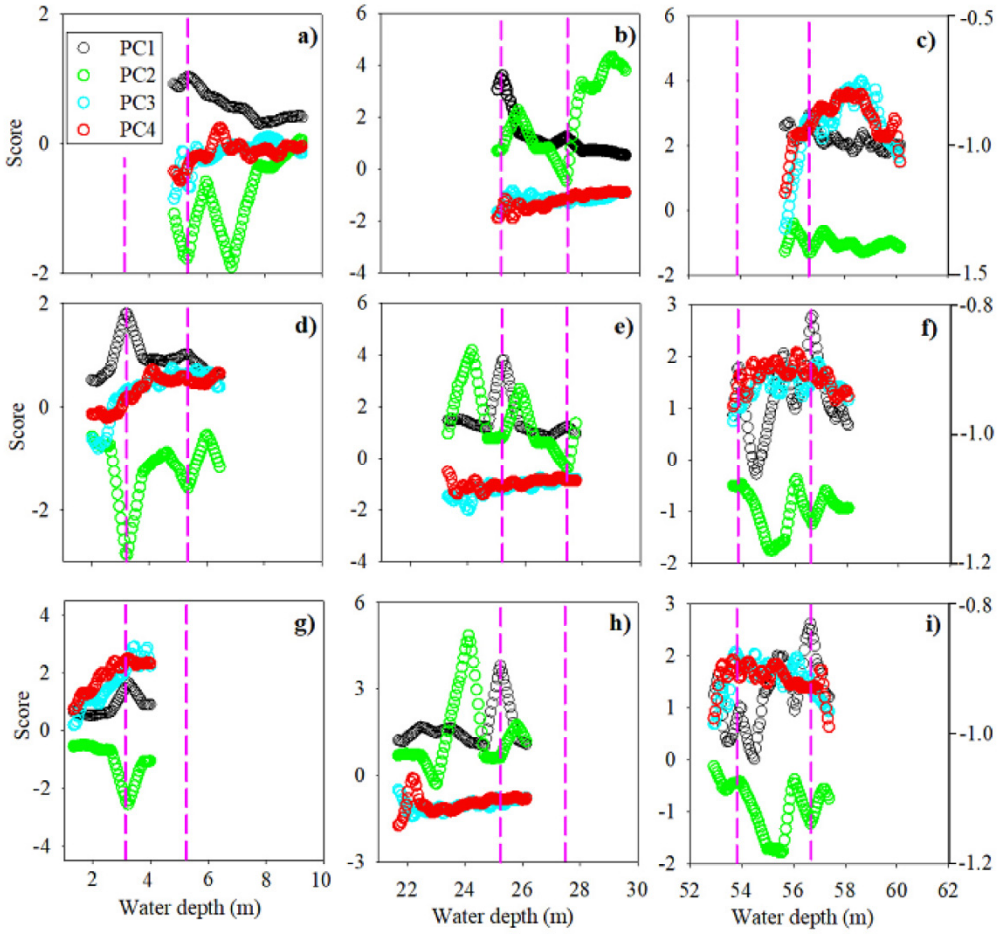

Fig. 5. PCA scores as a function of range to optical layers. Shallow, mid-depth and deep (left, center and right panels, respectively) PC1-derived layers (vertical dash lines). Far, intermediate and near position of FSUIL with respect to major PC1-derived discontinuities (upper, central and lower panels, respectively). PC1 scores for panels c,f and i (right y-axis).

As discussed before, these PC1 anomalies mainly reflect changes on non-polarized backscattering. Unlike Fig. 3, the vertical spacing between scores in Fig. 5 is 5.5 cm (i.e., 14-fold finer resolution than FSUIL depth differences between consecutive waveforms). That explains why the scattering peaks determined in Fig. 5 are not seen or barely distinguished in Fig. 3 where anomalies correspond to the first relative time bin of each waveform subset.

Optics EXPRESS

Also, these optical layers were difficult to detect or absent in vertical profiles of additional optical measurements (e.g., b_b) having a coarser spatial resolution (i.e., ~0.5 m) (Fig. 6(a)).

3.3. Layer detection and composition

In general, full range-resolved PC2-derived scores revealed an inverse covariation with respect with PC1 scores but at 53.9 m where scores changed in the same direction. Low PC2 scores usually matching the scattering layers suggest that strong vertical scattering discontinuities are characterized by high chlorophyll values as PC1 is inversely related to magnitude of non-polarized LiDAR backscattering. The correlation between PC1 and PC2 scores was not clearly related with LiDAR stand-off distance or water turbidity. To exemplify, the Spearman Rank correlation coefficient with an interval of confidence of 95% and for a layer located at 56.6 m was −0.973, −0.991 and −0.945 for a long, intermediate and short LiDAR stand-off distance, respectively. Also, additional analysis revealed that amplitude of PC1-derived scattering peaks as computed using peak-specific baselines was not related within the same waveform to the distance between the scattering layer and each receiver. Neither changes of amplitude seemed to be sensitive to FSUIL stand-off distances to the scattering layer as FSUIL was moving upward.

Optics EXPRESS

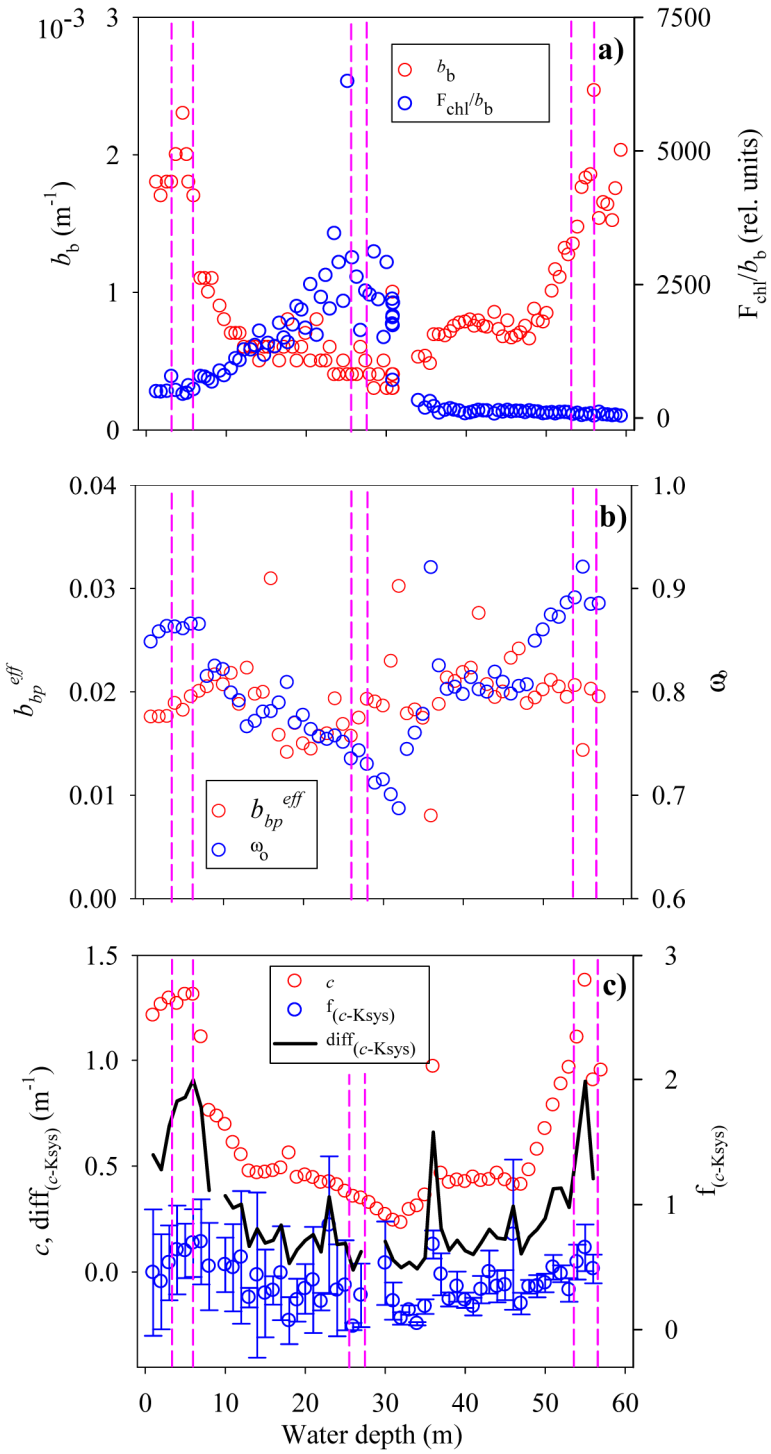

Fig. 6. Vertical profiles of ancillary optical variables. a) b_b (left y-axis), Fchl/b_b (right y-axis), b) b_{bp}^{eff} (left y-axis), ω_o (right y-axis), c) 1-m averaged c and diff(c-K_{sys}) (left y-axis), f(c-K_{sys}) (right y-axis). Uncertainty bars represent ± 2 standard errors. PC1-derived layers (vertical dash lines).

Optics EXPRESS

Vertical variability of range-resolved PC3 scores did not necessary follow changes on PC1 scores (e.g., mid-water peaks from 'close' position) (Fig. 5€). Indeed, direct (e.g., Fig. 5(i)) and inverse (e.g., Fig. 5(a)) covariations between PC1 and PC3 were identified within the same waveform or measurements obtained at different FSUIL locations. This suggests that scattering layers were not associated to typical low or high β^r values. This is consistent with the lack of concurrent vertical changes on PC1, b_{bp}^{eff} and ω_o (Fig. 6(b)). Similar to β^r, vertical variability of range-resolved PC4 scores did not reflect a clear correspondence with changes of PC1 scores. The depolarization ratio index was inversely related to PC1 scores in mid-water scattering peaks observed from a 'close' FSUIL position (Fig. 5(h)). However, this pattern disappeared as the LiDAR system was moving upward and approaching to the scattering feature situated at 25.3 m depth (Fig. 5(h)).

No high resolution c or K_{sys} values were available in this study to evaluate the influence of multiple scattering effects on layer detection and composition. However, ancillary data and FSUIL-derived K_{sys} estimates showed in general a strong covariation between diff(c - K_{sys}) and DRI values including at those locations where scattering layers were present (Fig. 3(d) to 6(c)). Although f(c - K_{sys}) tended to increase near the surface and toward the bottom of the vertical profile, no clear relationships were observed between f(c - K_{sys}) and DRI as function of water depth.

4. Discussion

The interpretation of results is organized in four main sub-sections encompassing the processing of raw waveforms including noise reduction techniques (1), the interrelation between principal components and optical proxies related to composition and size distribution of particulates (2), the range-resolved contribution of principal components to total variance (3), and the detection of scattering layers as a function of distance to the LiDAR receiver and water turbidity (4).

4.1. Denoising of LiDAR waveforms

A critical stage for developing accurate algorithms for finding and identifying submarine optical targets including strong spatial discontinuities is the quantification of measuring errors. Raw LiDAR backscattering measurements include two main kinds of noise that need to be removed before deconvolving each waveform: systematic and random uncertainties [27]. Random errors are related to the shot noise or noise originated from variations on the laser illumination and electromagnetic phenomena at the surface of the receiver (e.g., photoemission). These noise sources also include thermal fluctuations derived from different electro-optical components intervening during the light transmission and reception, random spikes caused by cosmic rays and non-deterministic variations originated from the digitizer.

Conversely, systematic noise comes from poor calibration, photodetector hysteresis, specific frequencies produced by electronic components and not related to the measurements and defective optical components. In terms of standard deviations, the application of wavelets reduced up to 3-fold the noise in 'off-water' and 'in-water' portions of selected waveforms. In general, the noise reduction of waveforms associated to different wavelets was more effective in ch_3 and at higher turbidities. The greater denoising of backscattering measurements made by ch_3 in turbid waters was associated to the smaller magnitude and variability of the signal arriving to ch_3 with respect to ch_1 and ch_2.

4.2. Interpretation of PCs variability

The largest contribution to PCA variance in this study was attributed to non-polarized LiDAR backscattering (i.e., total variability explained >60%). The impact of polarization changes as inferred from DRI was secondary due to the geometric configuration of the transmitter-receiver.

Optics EXPRESS

Polarization rotation due to a single scattering event can be described by a 16-element scattering matrix, which can be computed for a spherical particle with a known size and refractive index structure using Rayleigh-Gans approximation. However, typical oceanic particles vary in size, morphology, refractive index, and hence the theoretical predictions may have practical limitations for oceanic particles. Scattering matrices of collected samples representing a range of typical oceanic waters measured by Voss and Fry [28] show polarization-sensitive effects in some of the matrix elements, however, the measurement range (10° - 160°) does not extend to the scattering angles of FSUIL (179.1° and 178.4°). Linear depolarization ratios of an oceanic airborne LiDAR (i.e., ratio of scattering field intensities in the perpendicular and parallel directions to the original laser polarization plane) at angles near π has been found to responsive to the characteristics of bulk particle populations in coastal and open ocean environments [29], however, it has also been discussed that while the measurement of two orthogonal components of the airborne time-resolved backscattering signal may be an effective method to detect vertical structures within water column in an oceanic environment, the effect is likely to be also result of contributions from multiple forward- and back-scattering events in a relatively turbid environment [30]. Hence, the FSUIL depolarization measurement is expected to be most sensitive in a turbid environment or in environment where strong scattering layers are present.

Fchl was the main parameter altering PC2 even though an uncoupling between chlorophyll fluorescence anomalies and PC2 was detected in waters deeper than 51.5 m. PC2 scores associated to Fchl covaried directly with those corresponding to S_d^{ch1} (Coeff = 0.89 and 0.25, respectively). This suggests that relatively high LiDAR scattering returns were associated with high-chlorophyll measurements and viceversa. The lack of covariation between PC2 and Fchl in relatively deep waters was likely attributed to the dominant contribution of non-algal particulates (e.g. minerals, phytodetritus) to the LiDAR backscattering signal. Indeed, relatively low and constant Fchl to backscattering ratios as derived from concurrent backscattering coefficient measurements at 532 nm during the FSUIL surveys were calculated at depths greater than 37 m (Fig. 6(a)). The increase of turbidity/chlorophyll fluorescence ratios with depth has been reported in coastal waters of the Irish Sea where [31].

The β^r was the major source of variability of PC3 (Coeff = 0.82) and was inversely correlated with PC1 (Coeff = –0.40). Assuming a minor influence of pure seawater on vertical angular scattering changes, it is suggested that variations on volume scattering function and associated PC3 in this study was likely related to small-sized and/or mineral particulates. In general, the fraction of backward scattering increases as particulates have a smaller diameter and/or their chemical composition become enriched in inorganic matter [32]. Since the size of scatters increases with turbidity of natural waters, and particle forward-scattering at very low-angles (i.e., Fraunhofer diffraction) is directly related to the size of scatters [33], the backward scattering contributions as measured by FSUIL are less altered by modifications on particle size distributions if particle densities are relatively low.As *c* increases, the contribution of forward-scattered photons to total scattering is expected to increase. Thus, the influence of particle size will become more important as water turbidity increases.

4.3. Range-resolved variability of PCs

The general increase of PC1 contribution as a function of tr indicated an overall decrease of non-polarized backscattering with range. This phenomenon was mainly linked to the power attenuation of the LiDAR signal at longer optical paths. The curvature change and subsequent decrease of PC1 contribution between tr 31.7 and 40 ns was related to the shape of waveforms measured in ch_1, ch_2 and ch_3 and water samples characterized by relatively high turbidity levels. This effect was explained by the increase of multiple scattering toward

Optics EXPRESS

the trailing portion of the waveforms. As photons suffer a greater number of collisions, the backscattering signal is slightly augmented, thus the contribution of PC1 decreases.

Another physical process encompassing photons arriving to ch_2 and ch_3 receivers was the change of depolarization with range. This behavior was manifested as a general increase of PC4 contribution with distance to the LiDAR source. As the laser beam is travelling far from the source, higher orders of scattering become more prevalent due to particle and molecular collisions. In the near-range, single-backscattered photons at scattering angle of π dominate and depolarization is minor. Conversely in the far-range, optical paths and number of collisions increase, and the scattering directions of photons become more diffuse and less concentrated around the π direction. This should lead to an augmentation of DRI index values [29]. Lastly, range-resolved variation of PC4 contribution to total variance presented 'shoulders' (i.e., sharp increase or decrease of backscattered power) that were attributed to sharp changes on optical composition of the medium as FSUIL was moving upwards.

4.4. Full range-resolved PC scores

The remote detection of optical scattering layers by FSUIL was possible in waters encompassing a wide range of water turbidity (i.e., *c* variation 6-fold) and at distances to the receiver as long as 4.3 m. Anomalies in scattering- and absorption-related properties of optical layers were consistently identified based on high temporal resolution scores corresponding to PC1 and PC2, respectively. The use of PC3 and PC4 scores potentially provide finer detail regarding composition of the optical features. In general, the scattering layers were characterized by having a variable relationship between PC1-PC2 and PC3-PC4 scores. Regarding PC3, this suggests that composition of the layers was heterogeneous in terms of chemical composition likely associated to variations on particulate refractive index and particle size distribution affecting the volume scattering function [34]. Although having the same chlorophyll-a content, scattering layers may dramatically differ in terms of phytoplankton assemblages (e.g., diatoms vs flagellates) having contrasting particle size spectra and chemical composition (e.g., presence of biogenic silica or opal) [35].

Regarding PC4, high scores were expected to match high backscattering values as linear depolarization increases with scattering [28]. However, this pattern was not always observed as the largest DRI anomalies did not always coincide with the location of the scattering layers. LiDAR studies have shown that changes in layer internal structure and composition (e.g., spherical vs non-spherical scatterers) have a major influence on range-resolved behavior of LiDAR linear depolarization [28,29]. Thus, it is suggested that additional factors not considered in this study (e.g., particle shape, spatial distribution of optical components within the layer) were responsible of the lack of coherence between scattering layer positions, PC4 scores and associated DRI changes.

Vertical variability of diff(c - K_{sys}) and f(c - K_{sys}) values suggested that multiple scattering effects were positively linked to water turbidity and approximate location of scattering layers under investigation. Also, depth changes of f(c - K_{sys}) was less clear with respect to that associated to diff(c - K_{sys}) indicating that optical properties of particulates affecting the angular distribution of photons (e.g., chemical composition, particle size distribution, shape) had a secondary role on determining multiple scattering.

The vertical location of optical layers as inferred from the PCA technique was consistent with previous preliminary results using anomalies computed for each time bin of multiple waveforms obtained along the vertical. In this case, the vertical profile was made by descending the instrument with the laser shooting-downwards (i.e., nadir angle). Also, 100 instead of 80 time bins were processed by using the same reference time t_0 (i.e., absolute time bin = 40). Briefly, this filter (hereafter 'median' filter) is obtained by subtracting the median backscattering signal from each S_d value and normalizing the resulting difference by the standard deviation corresponding to that specific time bin (Fig. 11, Appendix). This 'median' filter showed the same main peaks derived from PCA and identified near the surface (e.g., 5-7

Optics EXPRESS

m) and the bottom (e.g., 55 m) by ch_3 and ch_1, respectively (Fig. 11a,c). Notice that median-based DRI anomalies were also useful to find surface layers (Fig. 11d). Despite this agreement, layer detection differences between the two techniques were found in some cases. In particular, the 'median' filter applied to ch_2 allowed a better visualization of relatively low-scattering/low-Fchl peaks at mid-depth (e.g., 38 m). Conversely, the contrast produced by the 'median' filter and backscattering signals derived from ch_1, ch_2 and ch_3 was insufficient to discriminate high Fchl features present at 25 m depth.

5. Conclusions

In the first part of this manuscript, a major effort was devoted to eliminate the system-related noise from the raw LiDAR backscattering signals derived from three channels encompassing different light polarization states. In the second part, the variability of the noise-free LiDAR signals was decomposed in orthogonal components and related to vertical changes of total scattering (i.e., water + particulates) at two angles, pigmented particulates using chlorophyll-a fluorescence as a proxy and depolarization of LiDAR backscattering in the π direction. Lastly, in the third section the focus was the detection of optical layers from different shooting distances and under contrasting turbidity conditions. Also, potential effects of multiple scattering and composition of particulates on discriminating these layers were discussed.

The detection of fine resolution optical features requires an optimization of the signal/noise ratios as the LiDAR backscattering signal decreases with range. Also, the minimization of random and systematic noise is critical for separating single from multiple scattering contributions and subsequent interpretation of microphysical properties of particulates. Here, the denoising was performed based on wavelets and was found to be dependent on the type of polarization and water turbidity.

Calculations based on the first relative time bin of each waveform subset suggested that total variability of principal components was driven by changes on non-polarized backscattering, a first-order parameter reflecting the power of the LiDAR return. Also, the strong correlation between b_b and S_d^{ch1} pointed out that particulate absorption had a secondary impact on vertical variability of LiDAR waveforms with respect to that attributed to particulate scattering. The use of β^r and DRI values did not seem to improve the characterization of layers in terms of composition. This difficulty highlights the large variability of second-order attributes (e.g., refractive index) of particulates within each scattering layer. Lastly, the detection of scattering layers did not necessary improve when the waveforms were generated closer to the layers and/or at lower turbidities due mainly to the rapid changes on inherent optical properties along as the LiDAR system was displaced upward. This contribution has two important findings. Firstly, the concurrent use of different signals associated to particulate absorption and scattering help to interpret the origin of the LiDAR backscattering and the mechanisms affecting the time/space variability of waveforms. Secondly, a non-invasive method was proposed and successfully evaluated to find and characterize scattering discontinuities under the sea. The suggested signal processing technique does not necessarily require vertical profiles and can be actually calibrated by using a fixed location and time series of ancillary optical information. Resulting time-resolved scores can be later applied in the same optical environment for detecting and discriminating multiple scattering targets at a fine resolution (i.e., ~5.6 cm) and optical depths as large as 4. Thus, the algorithm presented here is expected to be very useful for understanding patchiness, monitoring of subsurface oil spill features and localization of mines and military structures.

Optics EXPRESS

Appendix

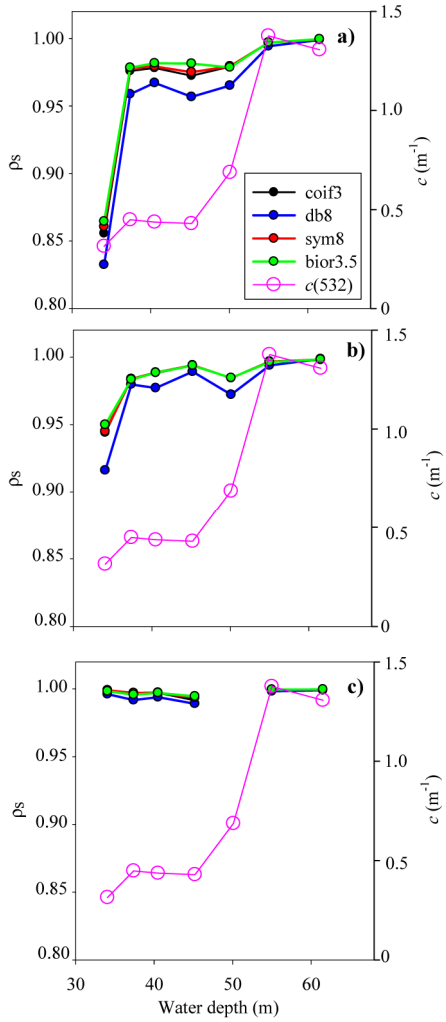

Fig. 7. Performance of wavelet denoising. a) ch_1, b) ch_2 and c) ch_3. Correlation coefficient between raw and denoised full waveforms (ρs) (left y-axis), depth-interpolated beam attenuation coefficient (*c* (right y-axis). Wavelets acronyms are defined in section 2.2.

Optics EXPRESS

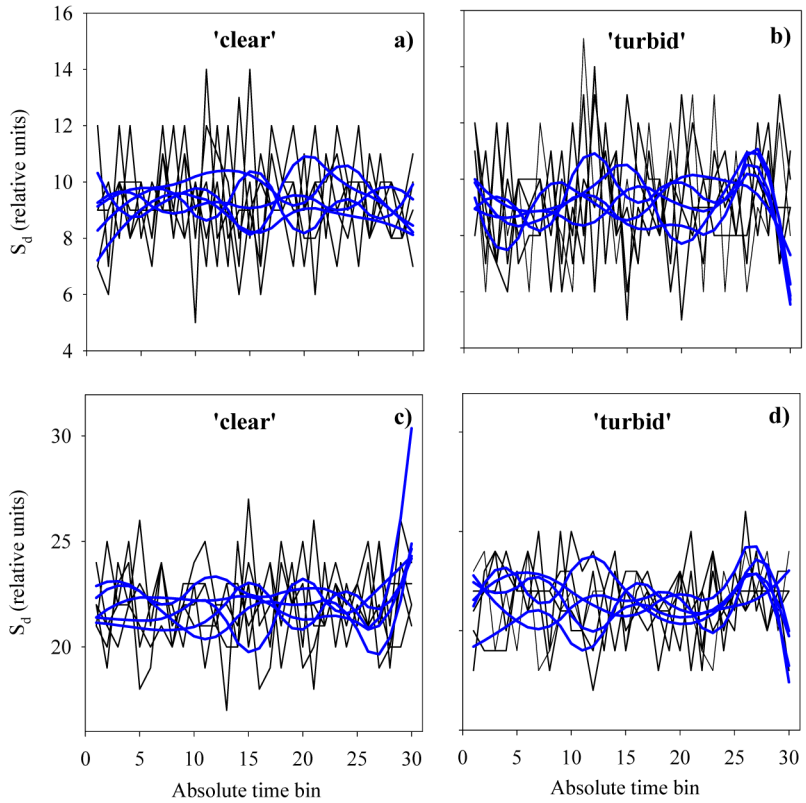

Fig. 8. Off-water noise of waveforms obtained at different water turbidities. a) and c) c = 0.26 m^{-1}, b) and d) c = 1.02 m^{-1}; ch_2 (upper panels), ch_3 (lower panels), raw (black line) and denoised (blue line) signal.

Optics EXPRESS

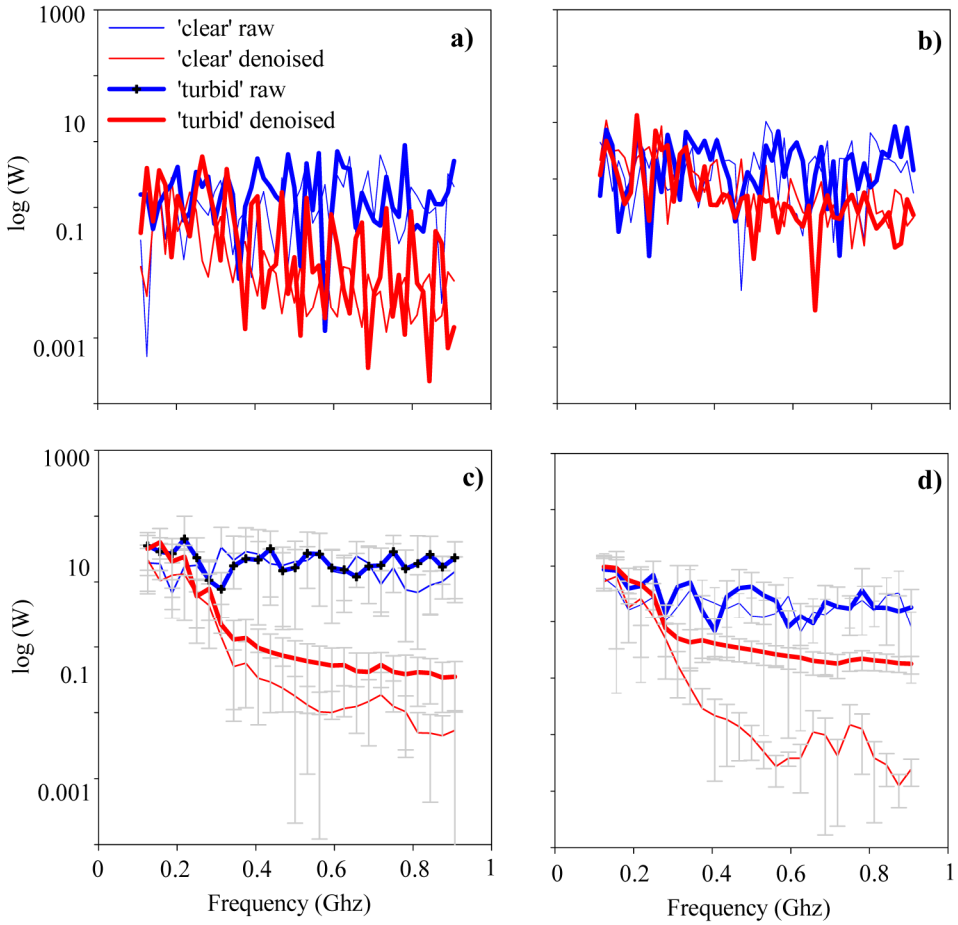

Fig. 9. Power spectra of noise (W) measured at different water turbidities. Off-water (upper panels), in-water (lower panels), ch_2 (left panels), ch_3 (right panels), W is the spectral density of the Fourier transform. Uncertainty bars are ± 2 standard errors.

Optics EXPRESS

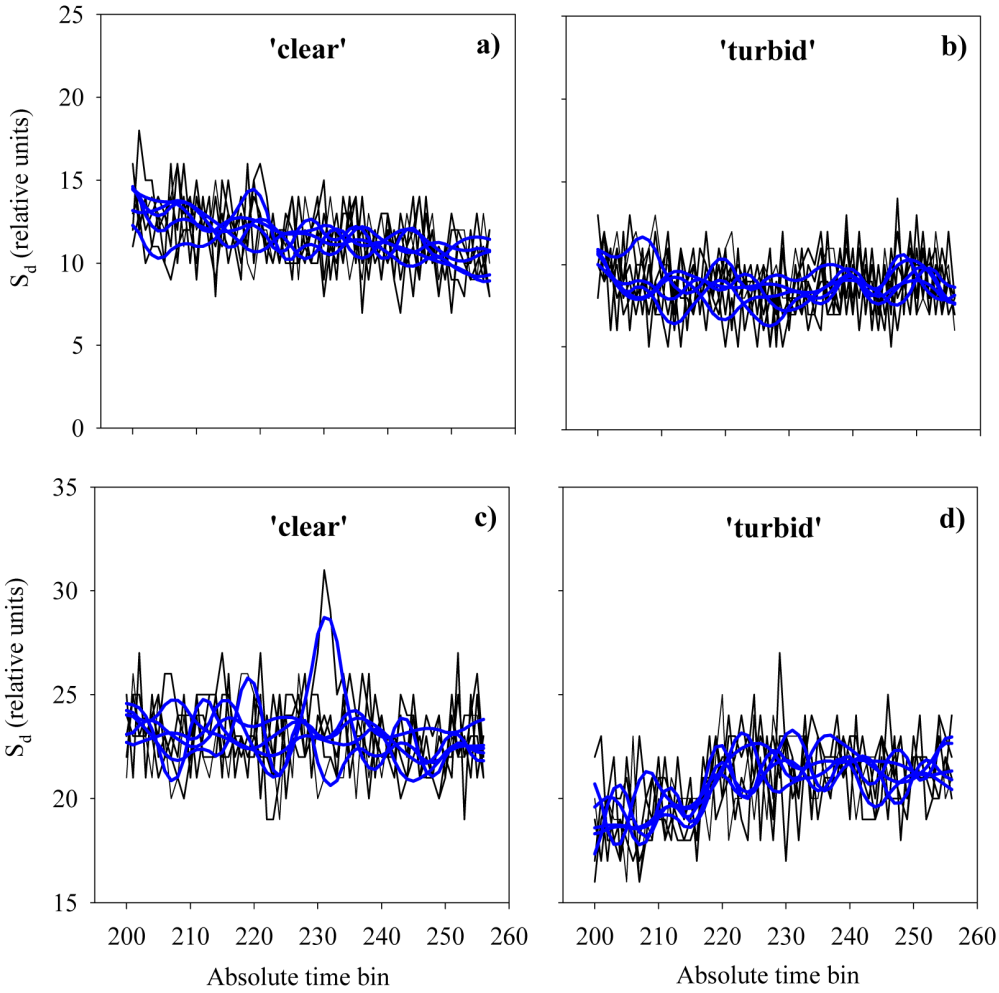

Fig. 10. In-water noise of waveforms obtained at different water turbidities. Turbidity cases and symbols as Fig. 8.

Optics EXPRESS

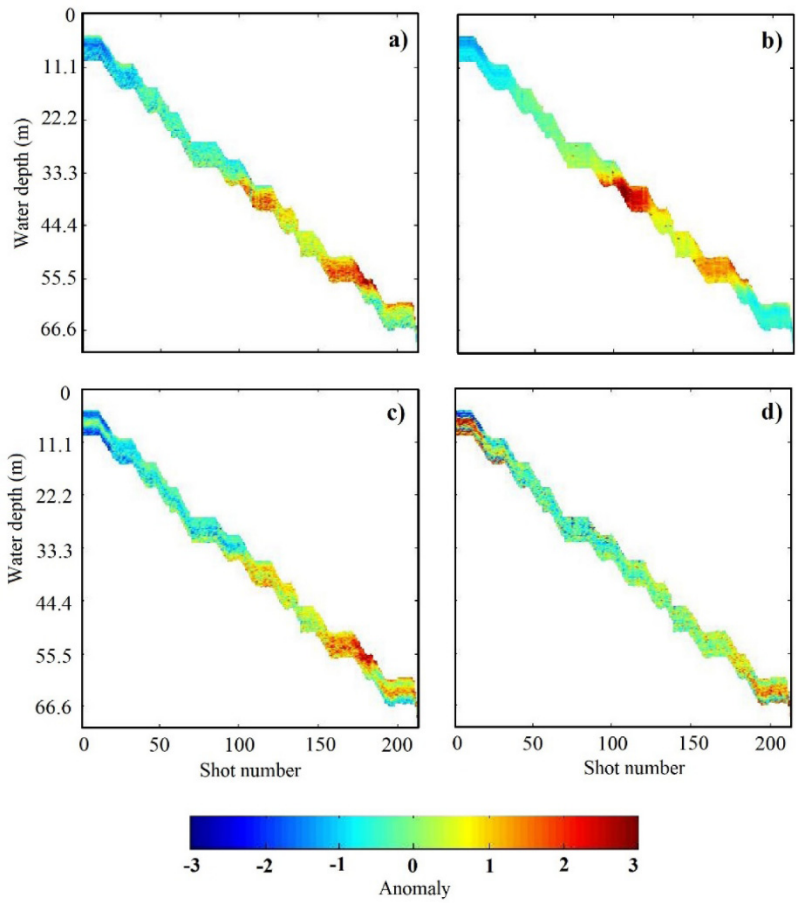

Fig. 11. Median filter anomalies of S_d as a function of water depth. a) ch_1, b) ch_2, c) ch_3 and d) DRI. Each shot generates 1 waveform.

Funding

Office of Naval Research (N00014-15-1-2608); National Oceanic and Atmospheric Administration (NA140AR4320260).

Acknowledgements

The development of FSUIL was supported by the Office of Naval Research, grant award number: N00014-15-1-2608 (PI: Fraser Dalgleish) and the NOAA award NA140AR4320260 to the Cooperative Institute for Ocean Exploration, Research and Technology (PI: Anni Vuorenkoski). We thank to HBOI technicians Brian Ramos and Benjamin Metzger for their technical and logistic support during the in situ surveys in the Gulf of Mexico.

References

1. Z. Lee, C. Hu, R. Arnone, and Z. Liu, "Impact of sub-pixel variations on ocean color remote sensing products," Opt. Express **20**(19), 20844–20854 (2012).
2. J. M. Sullivan, P. L. Donaghay, and J. E. B. Rines, "Coastal thin layer dynamics: Consequences to biology and optics," Cont. Shelf Res. **30**(1), 50–65 (2010).
3. J. H. Smart, "How accurately can we predict optical clarity in the littorals?" Johns Hopkins APL Tech. Dig. **25**(2), 112–120 (2004).
4. J. S. Jaffe, P. J. S. Franks, and A. W. Leising, "Simultaneous imaging of phytoplankton and zooplankton distributions," Oceanography (Wash. D.C.) **11**(1), 24–29 (1998).

Optics EXPRESS

5. D. G. Zawada and C. H. Mazel, "Fluorescence-based classification of Caribbean coral reef organisms and substrates," PLoS One **9**(1), e84570 (2014).
6. M. A. Montes-Hugo, J. H. Churnside, R. W. Gould, R. A. Arnone, and R. Foy, "Spatial coherence between remotely sensed ocean color data and vertical distribution of lidar backscattering in coastal stratified waters," Remote Sens. Environ. **114**(11), 2584–2593 (2010).
7. Z. Wang, S. F. DiMarco, S. Ingle, L. Belabbassi, and L. H. Al-Kharusi, "Seasonal and annual variability of vertically migrating scattering layers in the northern Arabian Sea," Deep Sea Res. Part I Oceanogr. Res. Pap. **90**, 152–165 (2014).
8. S. R. Pal, W. Steinbrecht, and A. I. Carswell, "Automated method for lidar determination of cloud-base height and vertical extent," Appl. Opt. **31**(10), 1488–1494 (1992).
9. M. A. Vaughan, S. A. Young, D. M. Winker, K. A. Powell, A. H. Omar, Z. Liu, Y. Hu, and C. A. Hostetler, "Fully automated analysis of space-based lidar data: an overview of the CALIPSO retrieval algorithms and data products," SPIE Proc. **5575**, doi. 10.1117/12.572024 (2004).
10. S. A. Young and M. A. Vaughan, "The retrieval of profiles of particulate extinction of cloud-aerosol Lidar infrared pathfinder satellite observations (CALIPSO) data: Algorithm description," Amer. Meteor. Soc. **26**, 1105–1119 (2013).
11. J.H. Churnside, and R.D. Marchbanks, "Subsurface plankton layers in the Arctic Ocean," Geoph. Res. Lett., **42**, 4896–4902.
12. A. K. Vuorenkoski, F. R. Dalgleish, M. S. Twardowski, B. Ouyang, and C. Trees, "Semi-empirical inversion technique for retrieval of quantitative attenuation profiles with underwater scanning LiDAR system," SPIE Conference Proceedings, Ocean Sensing and monitoring VII, ed. W. Hou, R. Arnone, **9459**, 1–6 (2015).
13. M. Misiti, Y. Misiti, G. Oppenheim, J. Poggi, *Wavelet toolbox for use with MATLAB*, Natick, MA, USA, Ver. 3.1 (MathWorks, Inc, 2006), p. 123.
14. are N. Al-Qazzaz, S. Hamid Bin Mohd Ali, S. Ahmad, M. Islam, and J. Escudero, "Selection of Mother Wavelet Functions for Multi-Channel EEG Signal Analysis during a Working Memory Task," Sensors (Basel) **15**(11), 29015–29035 (2015).
15. C. Spearman, "The proof and measurement of association between two things. By C. Spearman, 1904," Am. J. Psychol. **100**(3-4), 441–471 (1987).
16. G. C. Guenther, *Airborne Laser Hydrography: System Design and Performance Factors*, NOAA Professional Paper Series, National Ocean Service 1, (NOAA, 1985), ch 7, pp 188–201.
17. C. M. R. Platt,"Lidar and radiometric observations of cirrus clouds," J. Atmos. Sci. **30**(6), 1191–1204 (1973).
18. M. A. Montes, J. Churnside, Z. Lee, R. Gould, R. Arnone, and A. Weidemann, "Relationships between water attenuation coefficients derived from active and passive remote sensing: a case study from two coastal environments," Appl. Opt. **50**(18), 2990–2999 (2011).
19. D. Carr and G. Tuell, "Estimating field-of-view loss in bathymetric lidar: application to large-scale simulations," Appl. Opt. **53**(21), 4716–4721 (2014).
20. M. A. Montes-Hugo, A. K. Vuorenkoski, F. R. Dalgleish, and B. Ouyang, "Weibull approximation of LiDAR waveforms for estimating the beam attenuation coefficient," Opt. Express **24**(20), 22670–22681 (2016).
21. C. Moore, C. M. S. Twardowski, and J. R. V. Zaneveld, "The ECOVSF – A multi-angle scattering sensor for determination of the volume scattering function in the backward direction, "Proc. Ocean Optics XV, 16–20 October, Monaco, Office Naval Research, USA, CD-ROM (2000).
22. J. M. Sullivan, M. S. Twardowski, P. L. Donaghay, and S. A. Freeman, "Use of optical scattering to discriminate particle types in coastal waters," Appl. Opt. **44**(9), 1667 (2005).
23. E. Boss and W. S. Pegau, "Relationship of light scattering at an angle in the backward direction to the backscattering coefficient," Appl. Opt. **40**(30), 5503–5507 (2001).
24. A. Morel, "Optical properties of pure water and pure seawater," in: "*Optical aspects of Oceanography"*, edited by: N. G. Jerlov, and E. Steemann Nielson, New York, (Academic Press, 1974), 1–24 pp.
25. G. Mohammadpour, J. P. Gagné, P. Larouche, and M. A. Montes-Hugo, "is Optical properties of size fractions of suspended particulate matter in littoral waters of Québec," Biogeosciences Discuss. **14**(23), 5297–5312 (2017), doi: 10.5194/bg-14-5297-2017.
26. K. Pearson, "On Lines and Planes of Closest Fit to Systems of Points in Space," Philos. Mag. **2**(11), 559–572 (1901).
27. Z. Liu, W. Hunt, M. Vaughan, C. Hostetler, M. McGill, K. Powell, D. Winker, and Y. Hu, "Estimating random errors due to shot noise in backscatter lidar observations," Appl. Opt. **45**(18), 4437–4447 (2006).
28. K. J. Voss and E. S. Fry, "Measurement of the Mueller matrix for ocean water," Appl. Opt. **23**(23), 4427–4439 (1984).
29. J. H. Churnside, "Churnside, Polarization effects on oceanographic lidar," Opt. Express **16**(2), 1196–1207 (2008).
30. A. P. Vasilkov, Y. A. Goldin, B. A. Gureev, F. E. Hoge, R. N. Swift, and C. W. Wright, "Airborne polarized lidar detection of scattering layers in the ocean," Appl. Opt. **40**(24), 4353–4364 (2001).
31. D. McKee, A. Cunningham, and K. Jones, "Simultaneous Measurements of fluorescence and Beam Attenuation: Instrument Characterization and Interpretation of Signals from Stratified Coastal Waters," Estuar. Coast. Shelf Sci. **48**(1), 51–58 (1999).

Optics EXPRESS

32. X. Zhang, Y. Huot, D. J. Gray, A. Weidemann, and W. J. Rhea, "Biogeochemical origins of particles obtained from the inversion of the volume scattering function and spectral absorption in coastal waters," Biogeosc. **10**(9), 6029–6043 (2013).
33. Y. C. Agrawal and H. C. Pottsmith, "Laser diffraction particle sizing in STRESS," Cont. Shelf Res. **14**(10-11), 1101–1121 (1994).
34. M. S. Twardowski, E. Boss, J. B. Macdonald, W. S. Pegau, A. H. Barnard, and J. R. V. Zaneveld, "A model for estimating bulk refractive index from the optical backscattering ratio and the implications for understanding particle composition in case I and case II waters," J. Geophys. Res. **106**(C7 c7), 14129–14142 (2001).
35. J. M. Sullivan, P. L. Donaghay, and J. E. B. Rines, "Coastal thin layer dynamics: Consequences to biology and optics," Cont. Shelf Res. **30**(1), 50–65 (2010).